J. Space Weather Space Clim. 2025, **15**, 51
© R. Hajra et al., Published by EDP Sciences 2025
https://doi.org/10.1051/swsc/2025047

JSWSC
Available online at:
www.swsc-journal.org

Topical Issue – Severe space weather events of May 2024 and their impacts

RESEARCH ARTICLE OPEN ACCESS

Supersubstorms during the May 2024 superstorm

Rajkumar Hajra[1], Bruce T. Tsurutani[2], Quanming Lu[1], Aimin Du[3], and Gurbax S. Lakhina[4]

[1] CAS Key Laboratory of Geospace Environment, School of Earth and Space Sciences, University of Science and Technology of China, Hefei 230026, PR China
[2] Retired, Pasadena, California 91208, USA
[3] College of Earth and Planetary Sciences, Chinese Academy of Sciences, Beijing 100049, PR China
[4] Retired, Navi Mumbai 400703, India

Received 15 May 2025 / Accepted 10 October 2025

Abstract – We study in detail six isolated supersubstorms (SSSs; SML < − 2500 nT) during the May 2024 superstorm (SYM-H peak = −518 nT), the second largest storm by 1-min SYM-H index (since 1981). We also make comparisons to the largest and third largest magnetic storms, the March 1989 storm (SYM-H = −720 nT) and the November 2003 storm (SYM-H = −490 nT), respectively. Like the 1989 superstorm, the May 2024 superstorm is a complex event associated with multiple sheaths and magnetic clouds (MCs). However, unlike the 1989 superstorm, the May 2024 event had three MCs in the storm recovery phase with four SSSs. This caused the May 2024 event to have the longest and strongest "recovery phase" of the three storms. Because of this, the May 2024 event may be equally large in total energy as the 1989 storm. We revise previously published "tippy bucket" analyses for precursor energy input to assume a 3-h linearly input and subsequent dissipation of solar wind energy into the magnetosphere/magnetotail. The new linear tippy bucket model showed that the SSSs were triggered by the strong solar wind driving of ~ 10^{17} J. The Akasofu ε-parameter is used to estimate the solar wind energy input. All six SSS events could be explained by both precursor energy and direct driving. Two of the SSS events were possibly triggered by solar wind density parcels; the other four were not. The SSS events were highly varied in morphology, ranging from an isolated substorm morphology to a storm convection bay scenario. Overall, all six SSS events were unique. We suggest a two-mode nightside convection electric field to explain the nightside Joule heating variability. For the dayside Joule heating, we suggest three possible mechanisms: 1) adiabatic compression of magnetopause boundary layer plasma and dayside ionospheric precipitation, 2) deep penetration of solar wind protons and the generation of boundary layer field-aligned currents, and 3) magnetic reconnection with boundary layer magnetic fields with energy dissipation. It is noted that all three proposed mechanisms would deposit energy well away from the Earth's ionosphere. They are not measured by the ε-parameter either. The missing energy is due to the viscous interaction mechanism.

Keywords: Supersubstorm / Superstorm / Joule heating / Magnetic reconnection

1 Introduction

The 10–11 May 2024 superstorm (Hajra et al., 2024a) with a SYM-H peak intensity of −518 nT is the second largest storm by 1-min SYM-H index (since 1981), occurring ~ 35 years after the strongest event that occurred on 14 March 1989 (SYM-H peak = −720 nT; Allen et al., 1989; Bolduc, 2002; Chakraborty et al., 2008; Lakhina & Tsurutani, 2016; Boteler, 2019; Tsurutani et al., 2024) and ~ 21 years after the third strongest event on 20 November 2003 (SYM-H peak = −490 nT; Gopalswamy et al., 2005; Echer et al., 2008). It is worth mentioning that the May 2024 storm with a peak Dst = −412 nT is the seventh largest by Dst since the start of the space age in 1957, preceded by the storms peaking on 14 March 1989 (Dst = −589 nT), 13 March 1989 (−472 nT), 15 July 1959 (−429 nT), 13 September 1957 (−427 nT), 11 February 1958 (−426 nT), and 20 November 2003 (−422 nT). As can be seen from the SYM-H variations shown in Figures 1a–1c, compared to the 1989 and 2003 events, the 2024 event had the longest recovery with an enhanced ring current activity (note that the time scales on all three panels are the same). Integrated SYM-H during the recovery phase of the 2024 event is ~−442 nT.day, much greater than for the 1989 event

---

*Corresponding author: `rhajra@ustc.edu.cn; rajkumarhajra@yahoo.co.in`

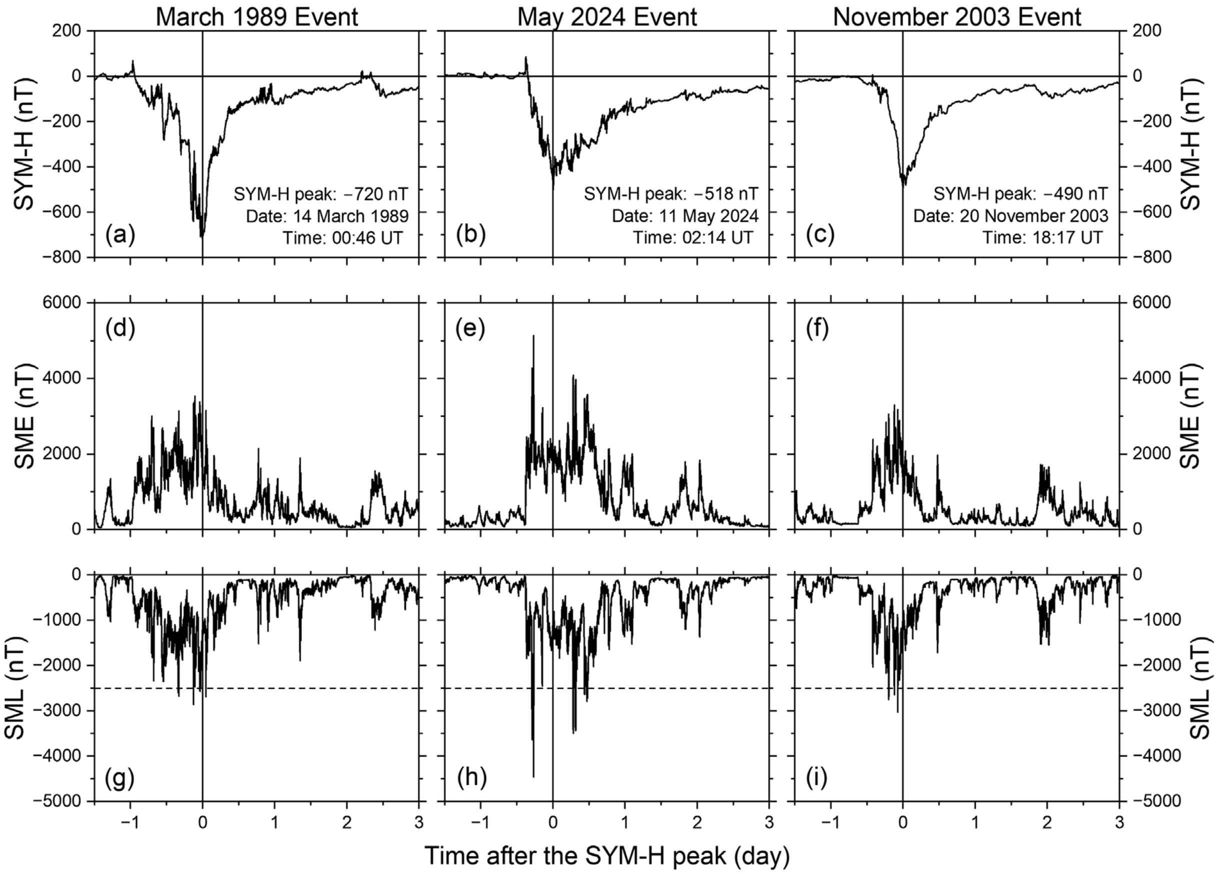

Figure 1. Three largest geomagnetic superstorms by SYM-H index (since 1981). From top to bottom, panels are (a–c) geomagnetic symmetric ring current index SYM-H, (d–f) auroral electrojet index SME, and (g–i) westward auroral electrojet index SML for the March 1989 storm (left panels), the May 2024 storm (middle panels), and the November 2003 storm (right panels). The *x*-axis indicates times in units of days after the onset of the SYM-H peaks mentioned in the top panels. Horizontal dashed lines in the bottom panels indicate the SML = −2500 nT level, the threshold for an SSS (Tsurutani et al., 2015).

(~−271 nT.day) and for the 2003 event (~−252 nT.day). Magnetospheric substorm activities during the main and recovery phases of the 2024 storm were significantly stronger in comparison to those during the 1989 and 2003 events. This effect can be noted in the variations of the SuperMAG auroral electrojet index SME (Figs. 1d–1f) and westward component SML (Figs. 1g–1i). We identified six supersubstorms (SSSs) characterized by the SML peak intensity < −2500 nT (Tsurutani et al., 2015), two during the main phase and four during the recovery phase of the May superstorm. Details of the SSSs are given in Table 1.

In Hajra et al. (2024a), we discussed the solar and interplanetary causes of the May 2024 superstorm and presented an overview of the storm's impacts on the magnetosphere-ionosphere coupled system. The purpose of the present paper is to study the SSSs during the superstorm. Previous case and statistical studies (Hajra et al., 2016, 2023; Hajra & Tsurutani, 2018) have established complex and distinct energy coupling processes of the SSSs. Recently, Tsurutani & Hajra (2023) showed cases where a single SSS accounts for the entire intense magnetic storm main phase energy. Thus, the study of SSSs might be important for a better understanding of the energy coupling (Dungey, 1961; Lu et al., 2022, 2025) of the extreme May event leading to significant impacts on the Earth's magnetosphere-ionosphere-atmosphere system, and even on the ground.

Here we summarize major impacts of the May 2024 superstorm and/or associated interplanetary phenomena. The outer radiation belt energetic (~keV– ~ MeV) electrons exhibited flux decreases (Hajra et al., 2024a). This can be explained through precipitation into the ionosphere (Zhou & Tsurutani, 1999; Tsurutani et al., 2016) or losses due to "magnetopause shadowing" (West et al., 1972, 1981) caused by a strong magnetospheric compression by an interplanetary shock (Tsurutani et al., 1988; Fu et al., 2025). The storm's main phase was associated with unusual early morning, daytime and evening time intensifications, and latitudinal and altitudinal expansions of ionospheric plasma anomaly (e.g., Aa et al., 2024; Bojilova et al., 2024; Carmo et al., 2024; Hajra et al., 2024a; Spogli et al., 2024; Sun et al., 2024; Themens et al., 2024; Hayakawa et al., 2025; Lee et al., 2025; Paul et al., 2025). These effects are assumed to be caused by an ionospheric "superfountain" associated with penetration of dawn-dusk directed interplanetary electric field (Tsurutani et al., 2004). A near-disappearance of the ionosphere was recorded during the storm recovery phase (Hajra et al., 2024a; Guo et al., 2024). The extreme storm caused global auroral sighting from exceptionally low magnetic

Table 1. Details of the SSSs identified during the May 2024 superstorm.

SSS number	Onset[a] (date UT)	SSS peak		Delay[b] (h)	Storm phase[c]
		SML intensity (nT)	Time (date UT)		
SSS 1	10 May 19:07	−3639	10 May 19:18	−6.92	MP
SSS 2	10 May 19:34	−4456	10 May 19:48	−6.42	MP
SSS 3	11 May 08:49	−3497	11 May 09:00	+6.77	RP
SSS 4	11 May 09:31	−3432	11 May 09:47	+7.57	RP
SSS 5	11 May 12:20	−2637	11 May 12:45	+10.52	RP
SSS 6	11 May 12:58	−2786	11 May 13:32	+11.30	RP

Notes. [a] Onset refers to the SSS expansion phase onset time determined from the sharp decrease in the SML index. [b] Delay is estimated from the occurrence time of the geomagnetic storm SYM-H peak = −518 nT to the SSS SML peak time. [c] MP and RP refer to the geomagnetic storm main phase and recovery phase, respectively.

latitudes (e.g., Carmo et al., 2024; Foster et al., 2024; Gonzalez-Esparza et al., 2024; Grandin et al., 2024; Nanjo & Shiokawa, 2024; Hayakawa et al., 2025; Lockwood et al., 2025), extreme intensification of the polar region field-aligned currents (FACs) and their equatorward expansion (Hajra et al., 2024a; Wang et al., 2024), and generation of strong geomagnetically induced currents (GICs) on ground conducting systems (Hajra et al., 2024a; Caraballo et al., 2025; Piersanti et al., 2025). While Zou et al. (2025) studied two of the SSSs (SSS 3 and SSS 4) in the 11 May 2024 superstorm recovery phase, there is no detailed study of the SSSs occurring during superstorms. We are conducting a more complete study involving two SSSs in the storm main phase and four in the storm recovery phase. We utilize measurements of near-Earth solar wind, polar region magnetometers and all-sky imaging to obtain a comprehensive understanding of solar wind-magnetosphere-ionosphere energy coupling associated with the SSSs. This study will hopefully increase our understanding of geophysical processes and the interpretation of the impacts of the May 2024 superstorm and extreme storms in general.

2 Data and methods

2.1 Data

This work is based on multi-instrument data analyses. The Wind spacecraft measurements (temporal resolution of 1 min) of the solar wind plasma and interplanetary magnetic fields (IMFs) obtained from NASA's Coordinated Data Analysis Web are explored to study the near-Earth interplanetary conditions. For a direct analysis of their impacts on the inner magnetosphere-ionosphere system, the Wind measurements are shifted in time to account for the solar wind propagation time from the spacecraft, at a geocentric distance of ~ 206–221 Earth radii (R_E, 1 R_E ~ 6371 km) upstream of the Earth, to the Earth's bow shock nose.

The geomagnetic conditions are studied by the SYM-H index (1-min resolution) collected from the World Data Center for Geomagnetism, Kyoto, Japan (Iyemori, 1990). SYM-H presents equatorial geomagnetic field perturbations mainly caused by westward ring currents encircling the Earth (in the magnetic equatorial plane) at ~ 2–7 R_E (Dessler & Parker, 1959; Sckopke, 1966). Auroral region substorm activity is explored by the SME and SML indices (1-min resolution) obtained from the SuperMAG database (Newell & Gjerloev, 2011). The SuperMAG network consists of ~ 300 magnetometers between (north hemispheric) 40° and 80° magnetic latitudes (Gjerloev, 2012). While SML is associated with substorm-related westward auroral electrojet current, SME is equivalent to the traditional (12-magnetometer-based) auroral electrojet index AE.

The substorm dynamics are studied by auroral region all-sky images (ASIs) and auroral movies obtained from the observatories Athabasca (geomagnetic latitude: 60.8°N, longitude: 51.5°W) and Lucky Lake (geomagnetic latitude: 58.2°N, longitude: 42.7°W), Canada. The auroral observations are made by highly sensitive, broadband, true color RGB (red, green, blue) Transition Region Explorer (TREx) sensors of the Canada Foundation for Innovation and the Canadian Space Agency, provided by the University of Calgary. However, we were able to collect the ASIs and auroral movies only from two observatories (mentioned above) and only for one of the six SSSs under this study.

2.2 Methods

Solar wind plasma and IMF parameters are used to identify upstream solar/interplanetary events/structures. Interplanetary fast forward (FF) shocks and waves are both characterized by sharp and simultaneous increases in the proton speed V_p, density N_p, ram pressure P_{sw}, proton temperature T_p, and IMF magnitude B_0 (Kennel et al., 1985; Tsurutani et al., 2011). Shocks are characterized by a magnetosonic Mach number $M_{ms} > 1$, while waves have $M_{ms} < 1$ (M_{ms} estimation is described in Hajra et al., 2024a).

Compressed plasma and IMF following the shock and wave are identified as signatures of interplanetary sheaths (Kennel et al., 1985; Tsurutani et al., 1988). Magnetic clouds (MCs) are identified by low T_p and low plasma-β (β representing ratio of the plasma pressure to the magnetic pressure), and slow and smooth rotations in IMF components B_x, B_y and B_z (Burlaga et al., 1981; Gonzalez & Tsurutani, 1987; Marubashi & Lepping, 2007).

The solar wind plasma and IMF parameters are used to estimate the motional electric field VB_s, where V represents V_p, and B_s is the southward component of IMF. We also computed the Akasofu ε-parameter (Perreault & Akasofu, 1978), an empirical estimate of the solar wind kinetic energy input rate into the magnetosphere:

$$\varepsilon = V_p B_0^2 \sin^4(\theta/2) R_{CF}^2, \qquad (1),$$

where θ is the IMF clock angle, and R_{CF} is the magnetopause scale size (Chapman & Ferraro, 1931):

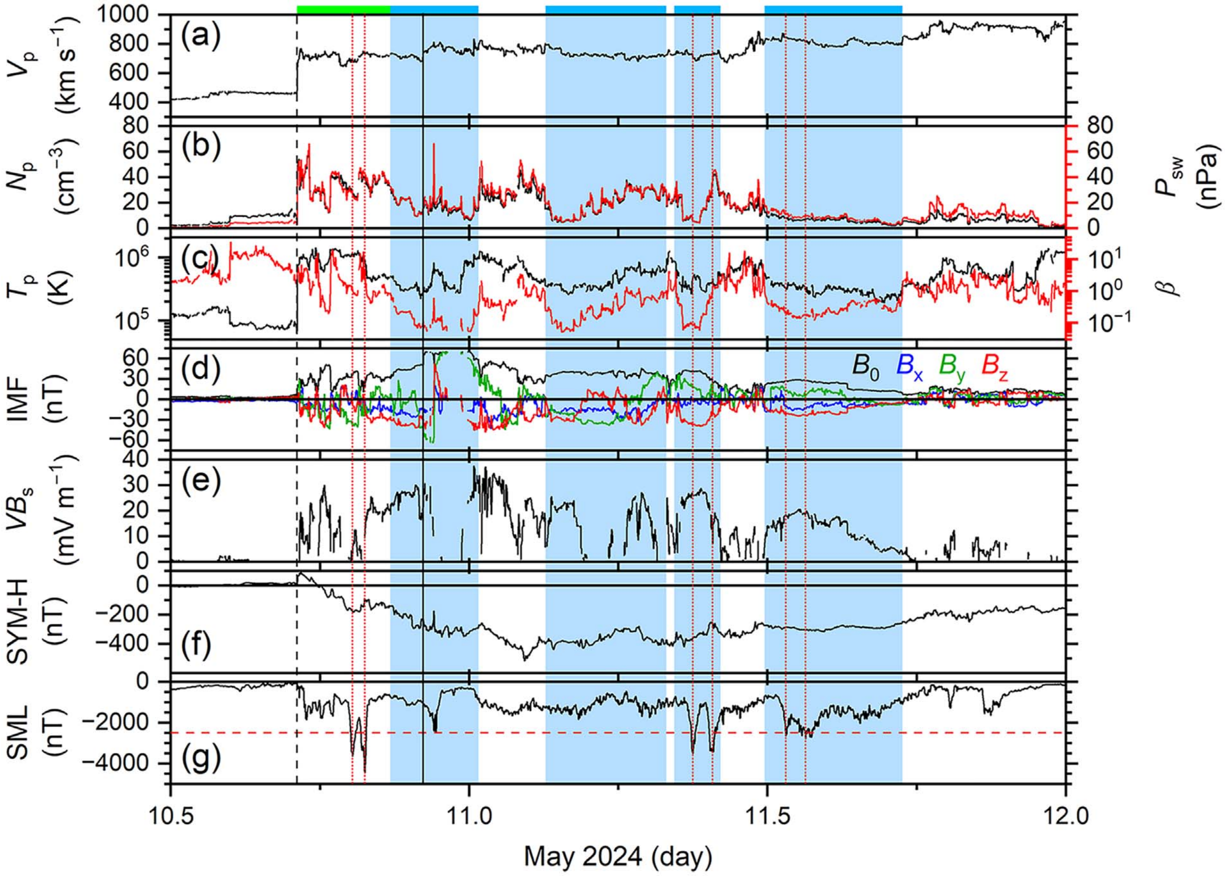

Figure 2. Solar wind, interplanetary and geomagnetic conditions during 10–11 May 2024. From top to bottom, the panels are: (a) solar wind proton speed V_p, (b) proton density N_p (black, legend on the left) and ram pressure P_{sw} (red, legend on the right), (c) proton temperature T_p (black, legend on the left) and plasma-β (red, legend on the right), (d) interplanetary magnetic field (IMF) magnitude B_0 (black), and B_x (blue), B_y (green), B_z (red) components, (e) motional electric field VB_s, (f) geomagnetic symmetric ring current index SYM-H, and (g) westward aurora electrojet index SML. Vertical lines indicate a fast forward (FF) shock (black dashed line), an FF wave (black solid line), and the SSS SML peaks (red short-dotted lines). An interplanetary sheath is marked by a green horizontal bar at the top, and magnetic clouds (MCs) are marked by light-blue vertical shadings and blue horizontal bars at the top. Red horizontal dashed line in the SML panel (g) indicates SML = −2500 nT, the threshold level for an SSS. The figure is updated from Hajra et al. (2024a).

$$R_{CF} = \left(2B_E^2/\left(\mu_0 m_p N_p V_p^2\right)\right)^{1/6} R_E, \tag{2}$$

B_E is the equatorial magnetic field on the Earth's surface, μ_0 is the free space permeability, and m_p is the proton mass.

Following previous studies (e.g., Turner et al., 2006; Guo et al., 2011; Hajra et al., 2014; Tsurutani & Hajra, 2023; Hajra et al., 2024a, 2024b), we estimated rates of the energy dissipation into the magnetospheric ring current (RC; Akasofu, 1981), and into the ionosphere through northern (summer) and southern (winter) hemispheric Joule heating (JH; Knipp et al., 2004) and auroral precipitation (AP; Akasofu, 1981) as follows:

$$P_{RC} = -4 \times 10^{13} \left(\frac{\partial \text{SYM-H}^*}{\partial t} + \frac{\text{SYM-H}^*}{\tau}\right), \tag{3}$$

$$P_{JH} = 42.63\,|\text{PC}| + 13.26\,\text{PC}^2 + 0.43\,|\text{SYM-H}| + 0.0137\,\text{SYM-H}^2, \tag{4}$$

$$P_{AP} = 10^8\,\text{SME}. \tag{5}$$

In the above expressions, SYM-H* is the solar wind pressure-corrected SYM-H (Burton et al., 1975):

$$\text{SYM-H}^* = \text{SYM-H} - 7.26 P_{sw}^{1/2} + 11, \tag{6}$$

τ is the average RC decay time, taken as 8 h for the present study (Yokoyama & Kamide, 1997; Guo et al., 2011), and PC is the polar cap potential index. Along with total ionospheric JH rates, magnetic local time (MLT)-dependent JH rates are computed in four 6-h long MLT sectors centered at 00:00 (21:00–03:00) MLT, 06:00 (03:00–09:00) MLT, 12:00 (09:00–15:00) MLT, and 18:00 (15:00–21:00) MLT using MLT-dependent symmetric ring current indices (Ohtani, 2021) obtained from SuperMAG.

To identify geomagnetic storms, we used the criteria of SYM-H peak < −50 nT (Gonzalez et al., 1994; originally defined by 1-h resolution Dst index). SSSs are identified using the criteria of SML peak < −2500 nT (Tsurutani et al., 2015).

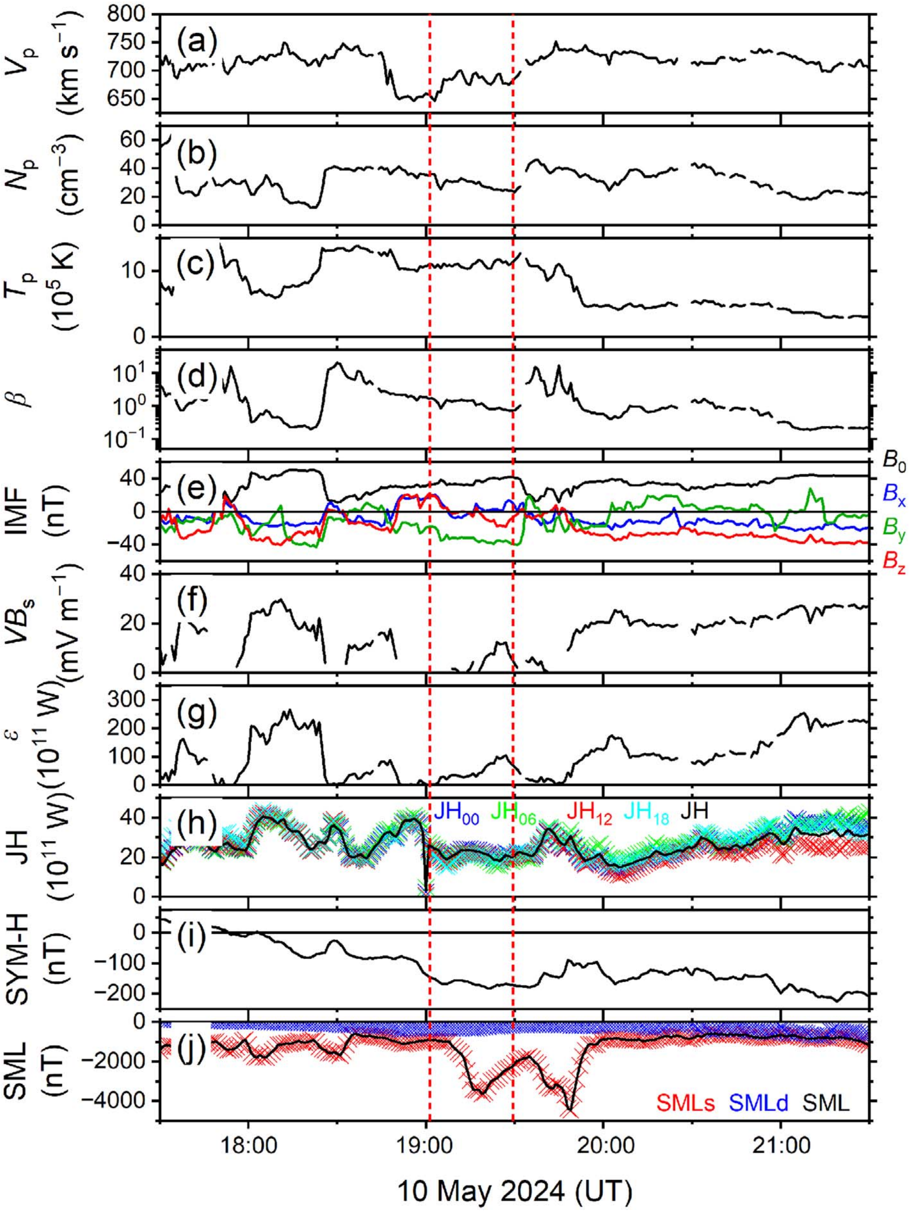

Figure 3. Interplanetary conditions and energy coupling associated with SSS 1 and SSS 2 during 10 May 2024 between 19:00 and 20:00 UT. From top to bottom, the panels are: (a) V_p, (b) N_p, (c) T_p, (d) β, (e) IMF B_0, B_x, B_y, and B_z, (f) VB_s, (g) the solar wind energy input rate/Akasofu ε-parameter; (h) the total JH rate (black), and the JH rates during 6-h long MLT sectors centered at 00:00 MLT (blue), 06:00 MLT (green), 12:00 MLT (red), and 18:00 MLT (cyan); (i) SYM-H, and (j) total SML (black), the sunlit ionospheric SML (SMLs, red), and the darkside SML (SMLd, blue). Vertical short-dashed red lines indicate the onset times of SSS 1 and SSS 2 expansion phases.

3 Results

3.1 The superstorm and the supersubstorms

Figure 2 shows the near-Earth solar wind plasma and IMF, along with geomagnetic indices during 10–11 May 2024. The SYM-H variation shows a complex geomagnetic storm, characterized by a sudden impulse (SI$^+$) amplitude of +88 nT at 17:15 UT on 10 May, followed by three successive decreases to −183 nT (at 19:21 UT on 10 May), −354 nT (at 23:12 UT on 10 May), and −518 nT (at 02:14 UT on 11 May) in a ~9-h long storm main phase, and subsequent ~3-day long recovery (Fig. 2f). The storm main and recovery phases are associated with very strong magnetospheric substorm activity, including six SSSs (Table 1), as indicated by the SML index variation (Fig. 2g). The SSS SML peaks are marked by vertical red short-dotted lines. The first two peaks (SSS 1, SSS 2) occurred during the magnetic storm main phase, ~−6.9 and −6.4 h relative to the strongest SYM-H peak occurrence, respectively. The other four SSS peaks (SSS 3, SSS 4, SSS 5, and SSS 6) occurred ~+6.8, +7.6, +10.5, and +11.3 h after the SYM-H peak, respectively, during the storm recovery phase. There is no apparent association between the SSS SML peak occurrences and the storm SYM-H intensifications. The SSS expansion phases, from the onset of the SML decrease to the SML peak, had durations of ~11, 14, 11, 17, 25, and

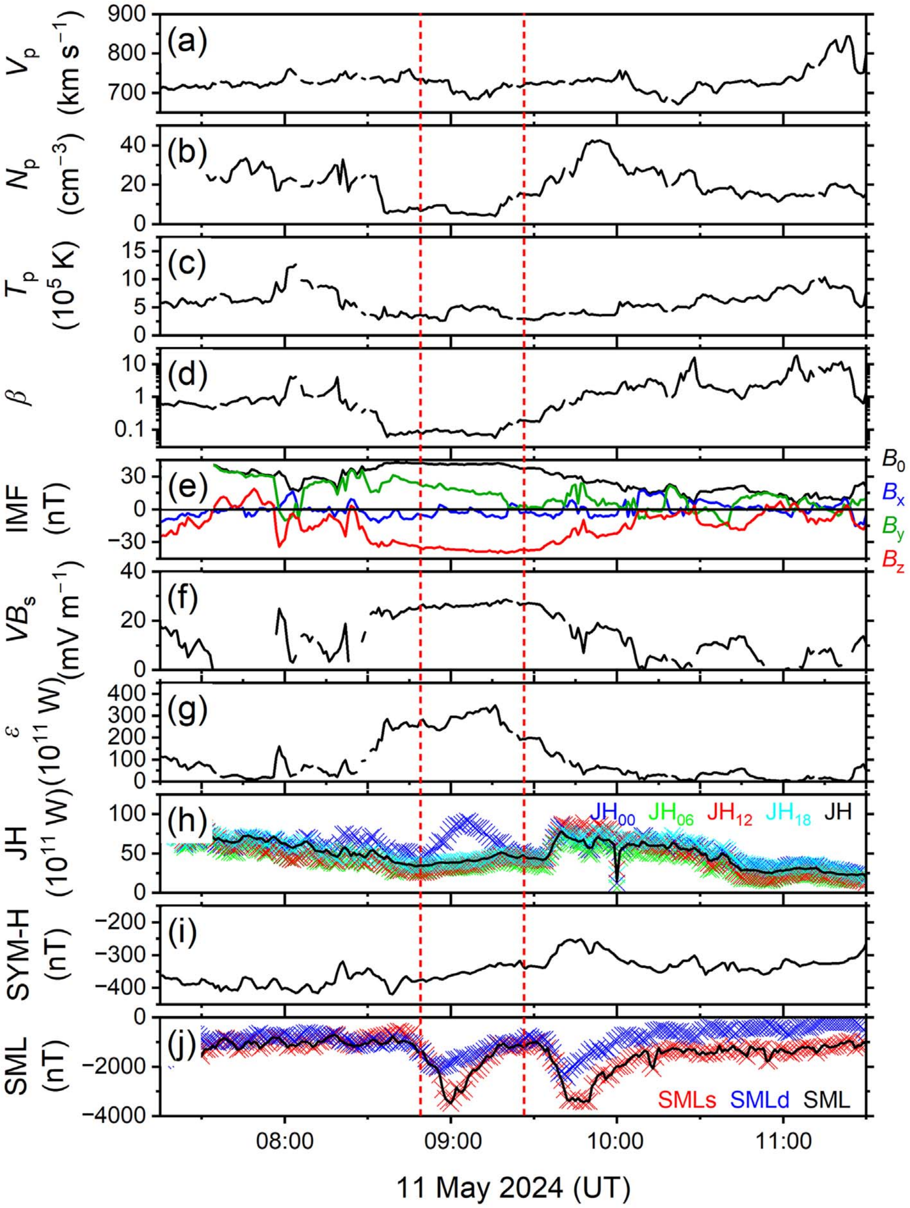

Figure 4. Interplanetary conditions and energy coupling associated with SSS 3 and SSS 4 during 11 May 2024 between 08:00 and 11:00 UT. Panels are in the same format as in Figure 3.

34 min, respectively. They are characterized by fast SML decreases at rates of −222, −179, −229, −132, −74, and −33 nT min^{-1}, respectively. It is interesting to note that the SSS expansion phase duration increased with time, the SSS intensity decreased, and the SML decreases became slower with time.

3.2 Interplanetary causes and energy coupling

A detailed study of the interplanetary conditions and their solar sources during the superstorm is presented in Hajra et al. (2024a). We mark the interplanetary structures in Figure 2 for reference. The SSSs occurring in the storm main phase (SSS 1, SSS 2) are associated with an interplanetary sheath (marked by a green horizontal bar at the top) extending from ~17:05 UT to ~20:50 UT on 10 May, which is characterized by fluctuating N_p, P_{sw}, T_p, and IMF components. Based on a detailed shock analysis (Rankine, 1870; Hugoniot, 1887, 1889; Abraham-Shrauner, 1972; Tsurutani & Lin, 1985), Hajra et al. (2024a) identified an FF shock with M_{ms} of ~7.2 at ~17:05 UT (marked by a vertical black dashed line), and a wave with M_{ms} of ~0.6 at ~22:09 UT on 10 May (marked by a vertical black solid line), leading to strong plasma and IMF compressions in the sheaths. From low T_p, β, and smooth IMF component variations, four MCs are identified from ~20:50 UT on 10 May to ~00:23 UT on 11 May, from ~03:05 UT to ~07:55 UT, from ~08:15 UT to ~10:07 UT, and from ~11:53 UT to ~17:26 UT on 11 May. These are marked by light-blue vertical shadings and blue horizontal bars at the top. The recovery phase SSSs (SSS 3, SSS 4, SSS 5, and SSS 6) are associated with the MCs.

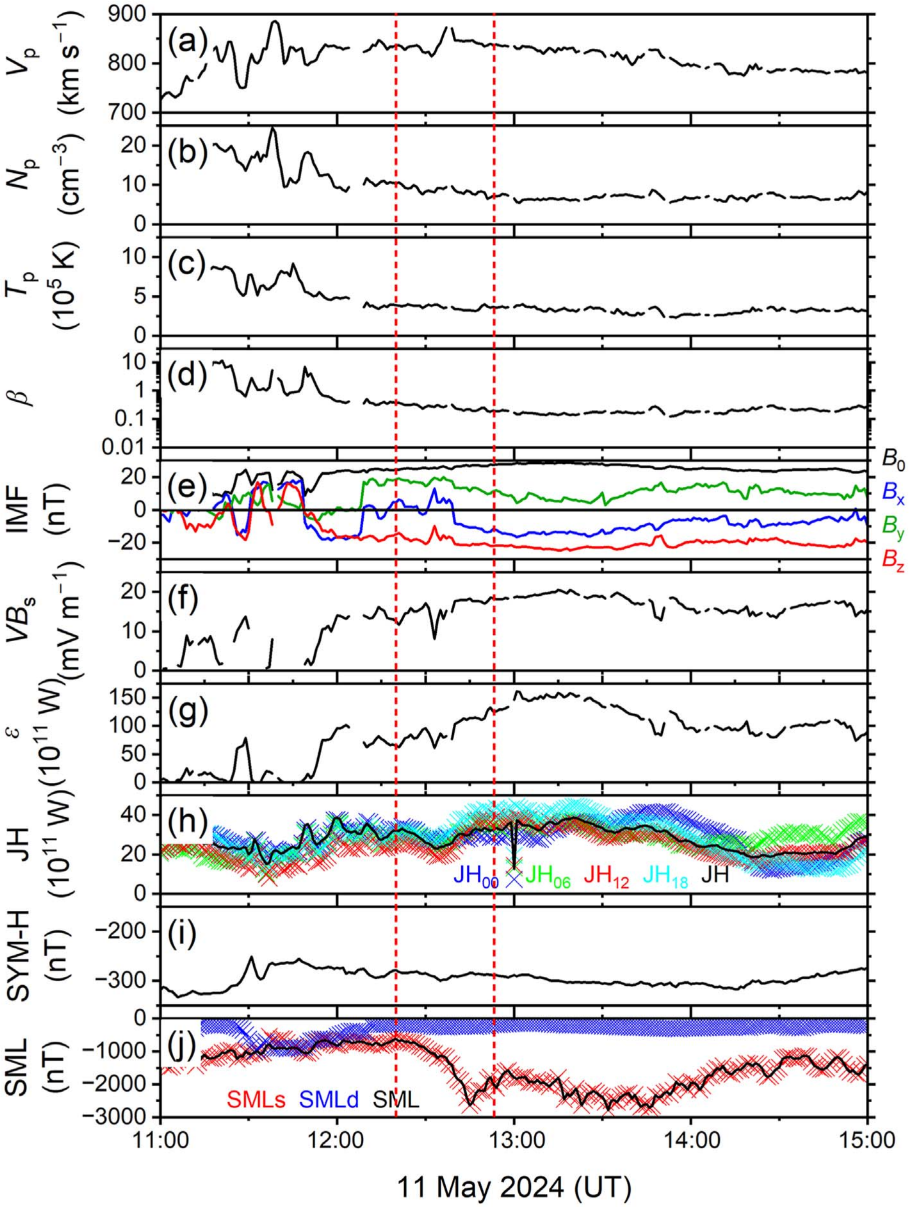

Figure 5. Interplanetary conditions and energy coupling associated with SSS 5 and SSS 6 during 11 May 2024 between 12:00 and 15:00 UT. Panels are in the same format as in Figure 3.

What are the interplanetary triggers for the six SSSs? To answer this question, solar wind plasma and IMF data for each of the events are closely studied in Figures 3, 4, and 5.

The SSS 1 expansion phase onset is marked by a sharp SML decrease at ~19:07 UT on 10 May, reaching an SML peak of −3639 nT at 19:18 UT, followed by a slower recovery (Fig. 3j). Interestingly, the SSS 1 SML is almost totally contributed by the sunlit ionosphere, and the darkside SML is insignificant. It should be noted that during May (northern hemispheric summer), most of the SML observatories are sunlit most of the day, even at magnetic midnight. Thus, we show the MLT distribution of SML for all SSSs in Appendix A, Figure A1. The strongest SML is observed in the morning MLT sector, between ~06:00 and 10:00 MLT (Fig. A1a). While SSS 1 occurred inside an interplanetary sheath (Fig. 3b), there is no immediate external trigger (pressure pulse or shock) at the SSS 1 onset. The onset is coincident with a small IMF southward turning, from $B_z = 0.3$ to -2.4 nT (Fig. 3e). During the SSS 1 expansion phase, the IMF (B_0 ~32 to 38 nT) was almost totally contributed by the B_y component (~−28 to −37 nT), while B_s (~6 nT), VB_s (~4 mV m^{-1}, Fig. 3f), magnetospheric reconnection energy input rate ε (~41 × 10^{11}, Fig. 3g) were low. The peak values of B_s (~18 nT), VB_s (~12 mV m^{-1}), and ε (~105 × 10^{11} W) were observed during the SSS 1 recovery phase. This may indicate direct energy driving during SSS 1.

Magnetospheric energy input during an SSS dissipates partly into the ionosphere through JH and AP and partly into the magnetospheric RC. The JH rate was more than one order of magnitude higher than the AP and RC dissipation rates (Appendix B Fig. B1); thus the latter are not shown in Figures 3–5. The peak

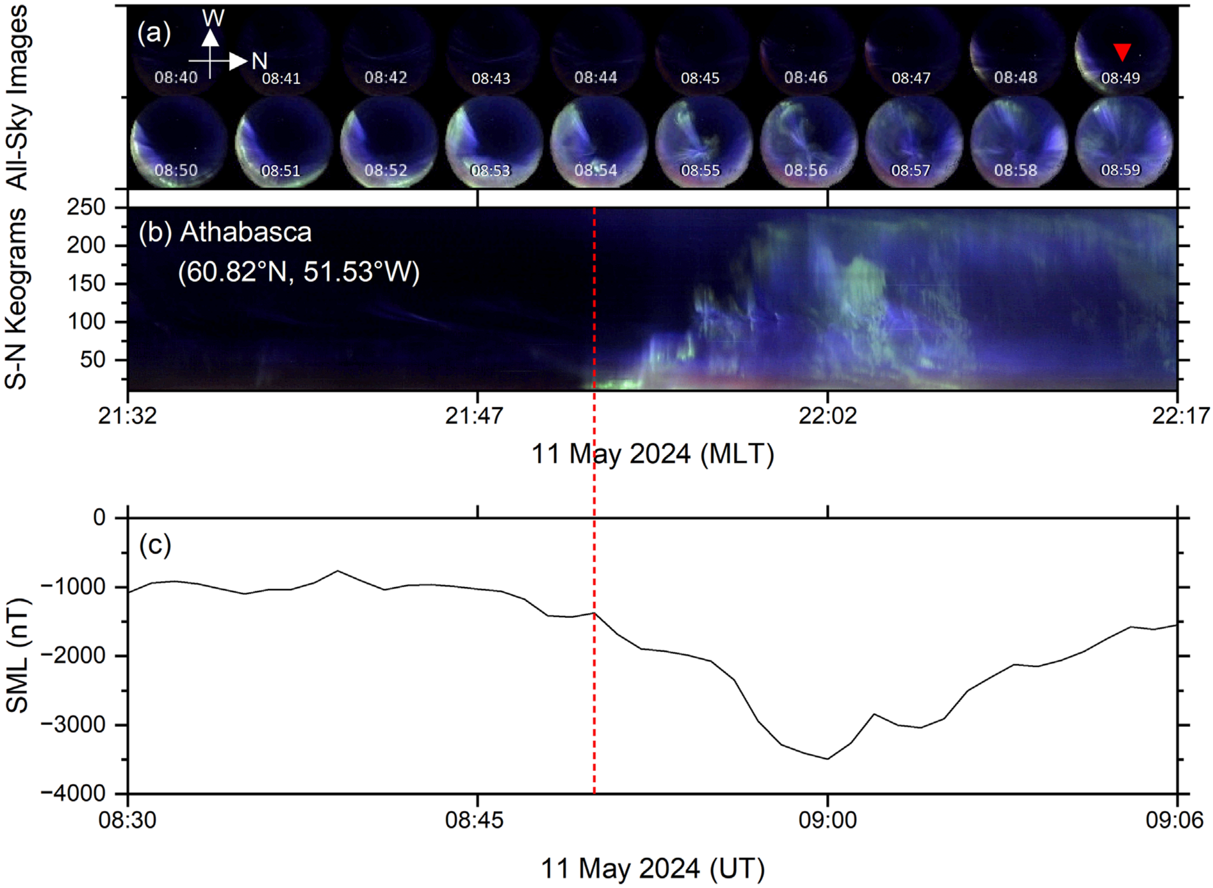

Figure 6. All-sky images (ASIs) at Athabasca, Canada, during SSS 3 on 11 May 2024. (a) ASI montages at every minute from 08:40 to 08:59 UT, directions are shown by arrows, UTs are mentioned for each of the ASIs; (b) ASI S-N keograms, Athabasca MLT is shown in the *x*-axis; and (c) SML variation. The substorm onset determined by the sharp SML decrease is marked by a vertical red short-dashed line, and the corresponding ASI is marked by a red downward arrow.

JH rate during SSS 1 was ~22 × 10^{11} W, with more or less similar JH rates at different MLT sectors (Fig. 3h).

While SSS 1 was recovering, the onset of the SSS 2 expansion phase was identified by a sharp SML decrease at 19:34 UT, SML reaching a peak intensity of −4456 nT at 19:48 UT on 10 May (Fig. 3j). It is one of the strongest SSSs in the SuperMAG record. The darkside SML is insignificant during this SSS as well (with the strongest SML in the ~06:00–10:00 MLT sector, see Fig. A1a). At the SSS 2 onset, IMF decreased in amplitude, turned southward following a brief ~1 min northward component, and B_y changed polarity from negative to positive (Fig. 3e). The SSS 2 expansion phase is associated with a weak B_s (VB_s) of ~9 nT (~6 mV m^{-1}). However, N_p (P_{sw}) exhibited a significant increase, by a factor of ~2, from a pre-SSS 2 value of ~23 cm^{-3} (~27 nPa) to ~46 cm^{-3} (~47 nPa) during the SSS 2 (Fig. 3f). Thus, the B_y polarity reversal and/or the plasma parcel (enhanced N_p/P_{sw}) may be considered as trigger(s) for the SSS 2. While the SSS 2 expansion phase was preceded by a strong energy input rate (ε peak ~105 × 10^{11} W), ε was low (~27 × 10^{11} W) during the expansion phase. However, the JH rate peaked (~34 × 10^{11} W) in the expansion phase and decreased gradually in the recovery phase when ε exhibited a gradual increase to ~174 × 10^{11} W.

The SSS 3 expansion phase onset at 08:49 UT on 11 May is marked by sharp decreases in both sunlit and darkside SML indices (Fig. 4j). However, while the darkside SML reached a peak of −2006 nT at ~08:55 UT followed by a gradual recovery, the sunlit SML exhibited further intensification leading to the SSS 3 peak SML intensity of −3497 nT at 09:00 UT (intense SML in the ~20:00–08:00 MLT sector, see Fig. A1b). The SSS 3 expansion phase onset was preceded by an IMF southward turning at 08:26 UT (Fig. 4e), followed by an almost stable IMF B_s (eastward VB_s; Fig. 4f) of ~36–37 nT (~21–28 mV m^{-1}) throughout the SSS 3, signifying both loading-unloading and direct energy driving for SSS 3. The energy input rate during the SSS 3 was significantly high, with a peak ε ~347 × 10^{11} W (Fig. 4g). Interestingly, the JH rates at 06:00, 12:00, and 18:00 MLT sectors exhibited a gradual increase during SSS 3, while the midnight (00:00 MLT) sector JH rate was significantly higher than those at other MLT sectors, and peaked to ~91 × 10^{11} W at 09:05 UT, slightly after the SSS 3 peak (Fig. 4h). For the SSS 3 event, we were unable to identify any “immediate” external trigger.

The SSS 4 expansion phase onset was recorded at 09:31 UT on 11 May, when the IMF B_s (and B_0) began to become weaker (Fig. 4e). However, the onset was coincident with a large N_p (P_{sw}) increase from a pre-SSS 4 value of ~14 cm^{-3}

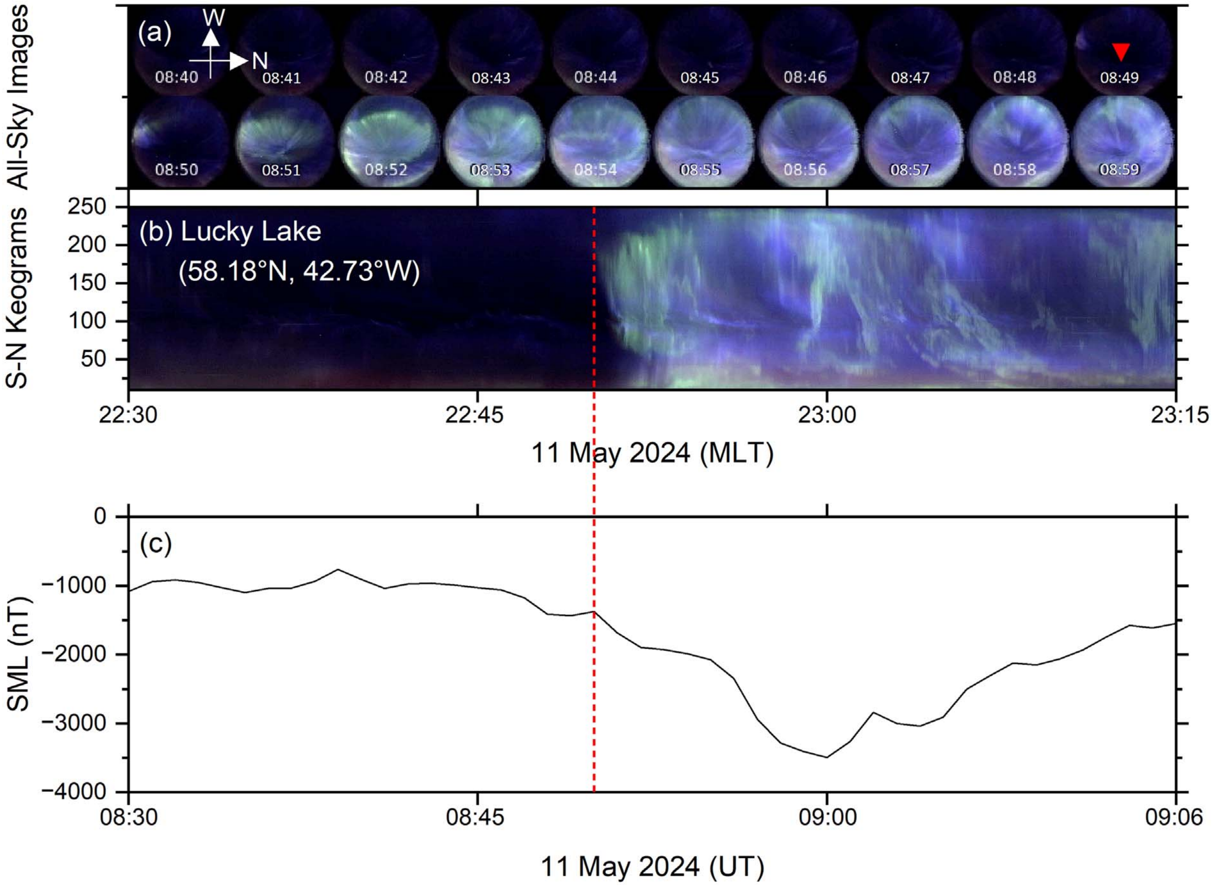

Figure 7. ASIs at Lucky Lake, Canada, during SSS 3 on 11 May 2024. Panels are in the same format as in Figure 6.

(~15 nPa) to a peak value of ~42 cm^{-3} (~46 nPa) during SSS 4 (Fig. 4b). Significant asymmetry is observed in the SSS 4 SML profile (Fig. 4j): While the darkside SML started decreasing after 09:39 UT, the sunlit SML exhibited a sharper intensification leading to overall SML intensification to −3432 nT at 09:47 UT (see Fig. A1b for MLT distribution of SML). While VB_s (Fig. 4f) and ε (Fig. 4g) exhibited gradual decreases following the SSS 4 onset, the SSS 4 expansion was associated with a sharp increase in the JH rates at different MLT sectors and a gradual decrease in the JH rates during the SSS 4 recovery phase (Fig. 4h).

The SSS 5 expansion phase onset is recorded at 12:20 UT on 11 May, followed by a gradual SML decrease leading to an SML peak of −2637 nT at 12:45 UT (Fig. 5j). The onset is preceded by an IMF southward turning at 11:49 UT (Fig. 5e), with a more or less stable B_s (VB_s; Fig. 5f) of ~21 nT (~18 mV m^{-1}), gradually increasing ε (Fig. 5g) and JH (Fig. 5h) rates during SSS 5. N_p (P_{sw}) was gradually decreasing during the SSS (Fig. 5b). While the SSS SML is dominantly attributed to sunlit SML (with the strongest SML in the ~02:00–10:00 MLT sector, see Fig. A1c), there are no apparent differences in JH rates at different MLT sectors.

The SSS 5 recovery is interrupted by the onset of SSS 6 at 12:58 UT on 11 May. The SSS 6 expansion is relatively gradual, peaking to −2786 nT at 13:32 UT (Fig. 5j). This SSS was associated with stable B_s (Fig. 5e), VB_s (Fig. 5f), and ε (Fig. 5g) and JH (Fig. 5h) rates. While the SSS SML is dominantly attributed to sunlit SML (see Fig. A1c), there are no apparent differences in the JH rates at different MLT sectors.

3.3 SSS imaging

Figure 6 shows selected ASIs (Fig. 6a) and ASI keograms (Fig. 6b) from Athabasca (geomagnetic latitude: 60.8°N, longitude: 51.5°W), Canada, during SSS 3 on 11 May (see Supplementary material Video S1 for corresponding auroral movie, which shows strong and violent auroral activities over the observatory). From 08:40 to 08:47 UT, the ASIs and the S-N keograms show almost clear sky without any auroral arc forming within the field-of-view of the instrument. The SSS 3 onset at 08:49 UT (based on the sharp SML decrease, Fig. 6c) is associated with a prominent auroral activation in the Athabasca keogram (at 21:51 MLT). A strong auroral signature is prominent in the southern part of the sky up to 08:52 UT (21:54 MLT). The auroral signatures are found to move poleward in the substorm expansion phase, followed by strong auroral activity above the instrument up to ~09:06 UT (22:08 MLT). Afterwards, auroral signatures are observed in the northern part of the sky. The auroral forms with well-defined sharp edges and significant brightness represent discrete aurora (e.g., Clausen & Nickisch, 2018).

The Lucky Lake (geomagnetic latitude: 58.2°N, longitude: 42.7°W) observatory, located southeast of Athabasca, registered the arc development ~1 min later, at 08:50 UT (Fig. 7a) (see Supplementary material Video S2 for corresponding auroral movie, which shows strong and violent auroral activities over the observatory). This time lag may imply equatorward movement of the auroras from Athabasca. Following the onset, the entire SSS 3 expansion and recovery phases are characterized by strong and dynamic auroral arcs (discrete aurora) in all directions, as confirmed by the keogram (Fig. 7b). Comparing keograms at Athabasca and Lucky Lake, equatorward expansion of the auroral activity can be inferred.

4 Summary

We presented a detailed study of six SSSs occurring during the 10–11 May 2024 geomagnetic superstorm. Near-Earth solar wind conditions and solar wind-magnetosphere coupling are explored using space and ground-based data for a comprehensive understanding of the events. The main findings are summarized below.

1. The May 2024 superstorm is an outlier, which has been caused by multiple solar flares and multiple coronal mass ejection (CME) releases (Hajra et al, 2024a), similar to the March 1989 superstorm event. The multiple sheaths and an MC led to the 1989 superstorm main phase to be the longest (~24 h) in history (Lakhina & Tsurutani, 2016; Boteler, 2019; Tsurutani et al., 2024), and here for the May 2024 superstorm, three MCs and four SSS events occurring after the peak SYM-H, have led this to have an extremely strong and long recovery phase (~3 days). Is this the longest recovery phase on record?
2. Among the six SSSs identified in this work, two (i.e., SSS 1 and SSS 2) occurred in the storm main phase, and four (i.e., SSS 3, SSS 4, SSS 5, and SSS 6) occurred in the storm recovery phase. The SSS SML peaks preceded or succeeded the superstorm SYM-H peak by more than 6 h. That is, the SSS occurrences and/or their (SML) intensities do not necessarily correlate with the superstorm (SYM-H) intensity. Hajra et al. (2016) showed that among seventy-four SSSs identified during 1981–2012, ~86% occurred during the magnetic storm main phase, 10% during the storm recovery phase, and 4% during geomagnetic quiet or not associated with any geomagnetic storms at all. In addition, Hajra et al. (2016) did not find any statistical correlations between SSS SML intensities with instantaneous SYM-H or storm SYM-H peak intensities. Interestingly, here we observed more SSSs in the recovery phase (four) than in the main phase (two), contrary to the Hajra et al. (2016) statistical result based on a large number of event studies.
3. Two SSSs occurring during the storm main phase were associated with an interplanetary sheath. Four SSSs occurring during the storm recovery phase were associated with interplanetary MCs. Statistically, ~54% of the SSSs are reported to be associated with interplanetary sheaths, and ~46% with MCs (Hajra et al., 2016; Despirak et al., 2019).
4. For four SSS events (SSS 1, SSS 2, SSS 5, and SSS 6), the SML intensifications were totally contributed by the sunlit ionosphere, while no SML intensifications were observed in the darkside of the globe. For two SSSs (SSS 3, and SSS 4), the darkside SML exhibited sharp increases during the SSS onsets, while the SML peak intensification was mainly recorded in the sunlitside. Are these results related to the fact that most of the stations were sunlit during the SSS events (occurring during May, northern hemispheric summer)? From the MLT-UT distributions of SML, the strongest SML is observed in the ~06:00–10:00 MLT sector for SSS 1 and SSS 2, and in the ~02:00–10:00 MLT sector for SSS 5 and SSS 6, while SML is found to intensify between ~20:00 and ~08:00 MLT during SSS 3 and SSS 4. These results clearly highlight distinguished characteristics of SSSs compared to nominal Akasofu (1964)-type substorms, where activities are suggested to be mainly magnetic midnight sector phenomena. It may be mentioned that Gjerloev et al. (2010) found, based on events and statistical analyses (including cases during northern hemispheric summer), that the SML-dark index showed no measurable response while the SML-sunlit index clearly intensified during substorm growth phase (following an IMF southward turning). They inferred a possible important role of ionospheric conductivity during the substorm growth phase. Present results seem to be consistent with the Gjerloev et al. (2010) results, but for the SSS expansion and recovery phases. Tsurutani & Gonzalez (2007) suggested that substorm magnetospheric convection electric fields are different from those related to geomagnetic storm convection bays. It is possible that in some cases the SSS electric fields are the same as the broad storm electric fields.

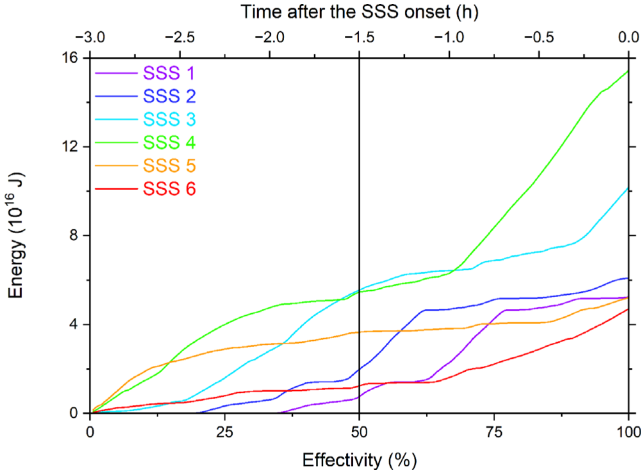

Figure 8. "Linear input tippy bucket" substorm model. Accumulated magnetic reconnection ε-energy starting from 3 h prior to the SSS onsets up to the onsets of the SSSs. Top x-axis marks the time in hours from the SSS onset, while bottom x-axis marks the linear effectivity of the accumulated energy in causing an SSS. The effectivity is assumed to increase linearly from 0% at 3 h prior to the SSS onset up to 100% at the SSS onset.

5. None of the SSSs was triggered by an interplanetary shock or a wave. Onsets of SSS 2 and SSS 4 were associated with plasma parcels characterized by strong N_p and P_{sw}, while there were no external triggers identified for other SSSs.
6. SSS 1 and SSS 2 were associated with a strong B_y field, while B_s, VB_s and ε were significantly low. B_y was

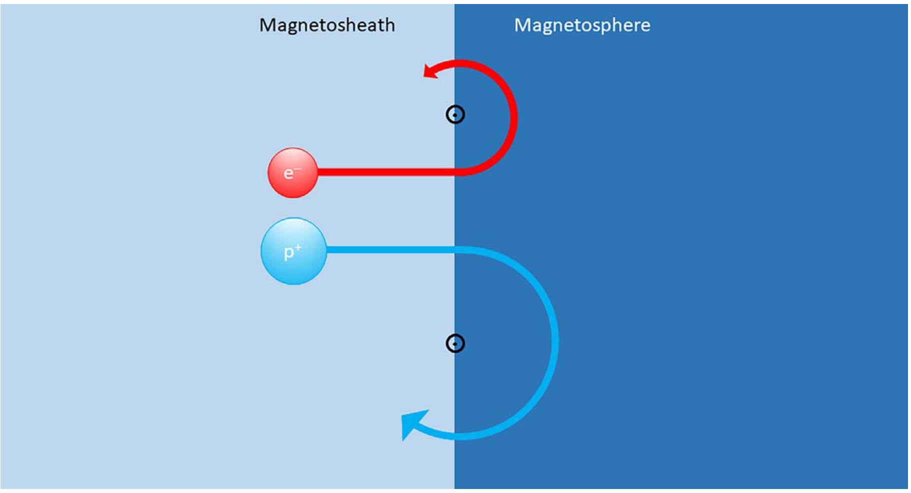

Figure 9. Schematic of ion (p^+) and electron (e^-) penetration, and consequent charge separation. Circles with dots in the center indicate magnetic fields pointing out from the plane of the page.

strongly negative during the entire SSS 1, while B_y sharply changed from negative to positive at the SSS 2 onset, and again from positive to negative during the expansion phase of SSS 2. Previous studies have discussed the important role of IMF B_y polarity on substorm occurrence rate (e.g., Hsu & McPherron, 2003; Liou et al., 2020; Ohma et al., 2021; Laitinen et al., 2024, and references therein). However, the physical mechanism of B_y impact is not well understood.

7. SSS 3, SSS 4, SSS 5, and SSS 6 were characterized by strong B_s, VB_s, and ε, indicative of a strong dayside magnetopause reconnection mechanism leading to magnetospheric energy flow and consequent SSSs.
8. Analysis of all-sky images from Athabasca (60.82°N, 51.53°W) and Lucky Lake (58.18°N, 42.73°W) in Canada during SSS 3 indicates the formation of discrete aurora with well-defined sharp edges and significant brightness. In the SSS expansion phase, the aurora exhibited a fast equatorward movement. Previously, Hajra & Tsurutani (2018) reported fast movement of SSS-related bright auroras from the pre-midnight sector to the post-midnight sector, which is consistent with the present result. Unfortunately, imaging data are not available for other SSSs under this study. Further studies of imaging data for more SSS cases are required for a better understanding of SSSs.

5 Discussion

Akasofu (2015) discussed the substorm energetics with a "tippy bucket" model. Accordingly, the low conductivity of quiet-time/pre-substorm ionosphere leads to accumulation of solar wind kinetic energy (when injected at a high rate of ~10^{11} W through magnetic reconnection) in the inner magnetosphere. However, when the accumulated energy reaches ~10^{16} J, the magnetosphere-ionosphere system becomes unstable and the accumulated energy is released impulsively, causing an auroral substorm (see also Akasofu, 2023). Zhou & Tsurutani (2001) suggested that southward IMF reconnection energy could provide substorm precursor energy up to ~1.5 h. Beyond this general time limit, the stored energy would have dissipated away. Based on the Akasofu (2015, 2023) and Zhou & Tsurutani (2001) works, here we introduce a modified, "linear input tippy bucket" substorm model. Figure 8 shows integrated ε-energy input starting from 3 h prior to the onset times of the six SSSs under this study. Considering that the probability of the SSS onset at 3 h prior to the actual onset is 0, and that probability is increased to 1.0 at the actual onset, it is assumed that the effectiveness (in causing an SSS) of the stored energy increases linearly from 0% at 3 h prior to 100% at the SSS onset.

The input energy effectiveness is found to increase with increasing energy input, as confirmed by Pearson's linear correlation coefficient *r*-values of 0.93, 0.97, 0.98, 0.95, 0.94, and 0.94 between the effectivity and input energy for SSS 1, SSS 2, SSS 3, SSS 4, SSS 5, and SSS 6, respectively. However, effective energy exhibits a large variation from one SSS to another. For example, the 50% effective energy is ~(1–2) × 10^{16} J for SSS 1, SSS 2, and SSS 6, it is ~4 × 10^{16} J for SSS 5, and ~5.5 × 10^{16} J for SSS 3 and SSS 4. The 100% effective energy is ~(5–6) × 10^{16} J for SSS 1, SSS 2, SSS 5, and SSS 6, ~10 × 10^{16} J for SSS 3, and ~15 × 10^{16} J for SSS 4. Thus, from our linear tippy bucket substorm model, it may be inferred that an accumulation of ~10^{17} J of solar wind kinetic energy in the magnetosphere seems to be effective in the impulsive occurrence of an SSS irrespective of an external trigger. It may be recalled that ~10^{16} J energy was empirically suggested to be an average energy required for a moderate-intensity substorm (Akasofu, 2023).

Two of the SSS onsets (SSS 2 and SSS 4) were preceded by solar wind plasma parcels characterized by strong ram pressure. Solar wind pressure pulses will cause compression of the dayside magnetopause boundary layer, energizing the boundary layer electrons and ions in $E_{\perp}$ direction (Zhou & Tsurutani, 1999). This solar wind ram energy input will be converted into plasma waves (Lakhina et al., 2000), which will scatter the boundary layer particles and lead to precipitation into the ionosphere, perhaps causing enhanced Joule heating noted in this paper. However, it should be noted that much of this energy input into the equatorial magnetopause might not reach the ionosphere. Much of this viscous interaction (Axford & Hines, 1961) will not be measured by current observational techniques as well (Tsurutani, 2024).

Higher solar wind plasma densities (in solar wind density pulses) or velocities (in shocks) will cause a greater abundance of solar wind ion penetration into the low latitude magnetopause boundary layer than solar wind electrons (see discussion in Tsurutani, 2024), leading to strong charge separation, as shown in Figure 9. This charge separation (deeper proton penetration into the magnetosphere) could lead to Joule heating all along the dayside magnetopause boundary layer.

What about SSS events that are not triggered by shocks/interplanetary plasma parcels or higher solar wind velocities? Magnetic reconnection at the dayside equatorial magnetopause may inject energy into the boundary layer with similar consequences to the above two mechanisms.

The above three possible mechanisms for energy input into the dayside magnetopause can all be explanations for enhanced Joule heating in the dayside ionosphere. Perhaps all three mechanisms are occurring at the same time. Dayside Joule heating has not been examined for isolated substorms. If it is found that dayside Joule heating occurs for isolated substorms, then perhaps all three mechanisms are occurring. However, if isolated substorms do not have dayside Joule heating in the equatorial magnetopause boundary layer, this will be an argument for viscous interaction energy input.

Acknowledgments

We would like to thank the reviewers and the editor for their extremely valuable suggestions that substantially improved the manuscript. The editor thanks two anonymous reviewers for their assistance in evaluating this paper.

Funding

The work of RH is funded by the “Hundred Talents Program” of the Chinese Academy of Sciences (CAS) and the “Excellent Young Scientists Fund Program (Overseas)” of the National Natural Science Foundation of China (NSFC).

Conflicts of interest

The authors declare no conflicts of interest.

Data availability statement

The Wind spacecraft measurements of the solar wind plasma and IMFs are obtained from NASA’s Coordinated Data Analysis Web (https://wind.nasa.gov/mfi_swe_plot.php). The geomagnetic SYM-H data are collected from the World Data Center for Geomagnetism, Kyoto, Japan (https://wdc.kugi.kyoto-u.ac.jp/). The SME and SML indices are obtained from the SuperMAG database (https://supermag.jhuapl.edu/indices/). The auroral region ASIs and auroral movies are obtained from the University of Calgary (https://www.ucalgary.ca/aurora).

Supplementary material

Supplementary Videos S1 and S2 show movies of auroral activities over Athabasca (geomagnetic latitude: 60.8°N, longitude: 51.5°W) and Lucky Lake (geomagnetic latitude: 58.2°N, longitude: 42.7°W), Canada, during SSS 3 that occurred in the recovery phase of the 2024 May superstorm. They show strong and violent auroral activities over the observatories.

The supplementary materials of this article are available at https://www.swsc-journal.org/10.1051/swsc/2025047/olm.

References

Aa, E, Chen Y, Luo B. 2024. Dynamic expansion and merging of the equatorial ionization anomaly during the 10–11 May 2024 super geomagnetic storm. *Remote Sens* **16**: 4290. https://doi.org/10.3390/rs16224290.

Abraham-Shrauner, B. 1972. Determination of magnetohydrodynamic shock normal. *J Geophys Res* **77**: 736–739. https://doi.org/10.1029/JA077i004p00736.

Akasofu, SI. 1981. Energy coupling between the solar wind and the magnetosphere. *Space Science Rev* **28**: 121–190. https://doi.org/10.1007/BF00218810.

Akasofu, SI. 1964. The development of the auroral substorm. *Planet Space Sci* **12**: 273–282. https://doi.org/10.1016/0032-0633(64)90151-5.

Akasofu, SI. 2015. Auroral substorms as an electrical discharge phenomenon. *Prog Earth Planet Sci* **2**: 20. https://doi.org/10.1186/s40645-015-0050-9.

Akasofu, SI. 2023. A new understanding of why the aurora has explosive characteristics. *Month Not Royal Astronom Soc* **518**: 3286–3300. https://doi.org/10.1093/mnras/stac3187.

Allen, J, Sauer H, Frank L, Reiff P. 1989. Effects of the March 1989 solar activity. *Eos Trans AGU* **70**: 1479–1488. https://doi.org/10.1029/89EO00409.

Axford, WI, Hines CO. 1961. A unifying theory of high-latitude geophyaical phenomena and geomagnetic storms. *Canadian J Phys* **39**: 1433–1464. https://doi.org/10.1139/p61-172.

Bojilova, R, Mukhtarov P, Pancheva D. 2024. Global ionospheric response during extreme geomagnetic storm in May 2024. *Remote Sens* **16**: 4046. https://doi.org/10.3390/rs16214046.

Bolduc, L. 2002. GIC observations and studies in the Hydro-Québec power system. *J Atmos Sol Terr Phys* **64**: 1793–1802. https://doi.org/10.1016/S1364-6826(02)00128-1.

Boteler, DH. 2019. A 21st century view of the March 1989 magnetic storm. *Space Weather* **17**: 1427–1441. https://doi.org/10.1029/2019SW002278.

Burlaga, L, Sittler E, Mariani F, Schwenn R. 1981. Magnetic loop behind an interplanetary shock: Voyager, Helios, and IMP 8 observations. *J Geophys Res Space Phys* **86**: 6673–6684. https://doi.org/10.1029/JA086iA08p06673.

Burton, RK, McPherron RL, Russell CT. 1975. An empirical relationship between interplanetary conditions and Dst. *J Geophys Res* **80**: 4204–4214. https://doi.org/10.1029/JA080i031p04204.

Caraballo, R, González-Esparza JA, Pacheco CR, Corona-Romero P, Arzate-Flores JA, et al. 2025. The impact of geomagnetically induced currents (GIC) on the Mexican power grid: numerical modeling and observations from the 10 May 2024, geomagnetic storm. *Geophys Res Lett* **52**: e2024GL112749. https://doi.org/10.1029/2024GL112749.

Carmo, CS, Dai L, Wrasse CM, Barros D, Takahashi H, et al. 2024. Ionospheric response to the extreme 2024 Mother’s Day geomagnetic storm over the latin American sector. *Space Weather* **22**: e2024SW004054. https://doi.org/10.1029/2024SW004054.

Chakraborty, SK, Hajra R, Paul A. 2008. Ionosphere near the anomaly crest in Indian zone during magnetic storm on 13–14 March 1989. *Ind J Radio Space Phys* **37**: 396–407. http://nopr.niscpr.res.in/handle/123456789/2775.

Chapman, S, Ferraro VCA. 1931. A new theory of magnetic storms. *Terres Magn Atmos Electr* **36**: 77–97. https://doi.org/10.1029/TE036i002p00077.

Clausen, LBN, Nickisch H. 2018. Automatic classification of auroral images from the oslo auroral themis (OATH) data set using machine learning. *J Geophys Res Space Phys* **123**: 5640–5647. https://doi.org/10.1029/2018JA025274.

Despirak, IV, Lyubchich AA, Kleimenova NG. 2019. Supersubstorms and conditions in the solar wind. *Geomag Aeron* **59**: 170–176. https://doi.org/10.1134/S0016793219020075.

Dessler, AJ, Parker EN. 1959. Hydromagnetic theory of geomagnetic storms. *J Geophys Res* **64**: 2239–2252. https://doi.org/10.1029/JZ064i012p02239.

Dungey, JW. 1961. Interplanetary magnetic field and the auroral zones. *Phys Rev Lett* **6**: 47–48. https://doi.org/10.1103/PhysRev Lett.6.47.

Echer, E, Gonzalez WD, Tsurutani BT. 2008.. Interplanetary conditions leading to superintense geomagnetic storms (Dst ≤ -250 nT) during solar cycle 23. *Geophys Res Lett* **35**: L06S03. https://doi.org/10.1029/2007GL031755.

Foster, JC, Erickson PJ, Nishimura Y, Zhang SR, Bush DC, et al. 2024. Imaging the May 2024 extreme aurora with ionospheric total electron content. *Geophys Res Lett* **51**: e2024GL111981. https://doi.org/10.1029/2024GL111981.

Fu, WD, Fu HS, Zhang WZ, Yu Y, Cao JB. 2025. Compression of Earth's magnetopause down to 5 R_E during the superstorm on 10 May 2024. *Geophys Res Lett* **52**: e2024GL114040. https://doi.org/10.1029/2024GL114040.

Gjerloev, JW, Hoffman RA, Ohtani S, Weygand J, Barnes R. 2010. Response of the auroral electrojet indices to abrupt southward IMF turnings. *Ann Geophys* **28**: 1167–1182. https://doi.org/10.5194/angeo-28-1167-2010.

Gjerloev, JW. 2012. The SuperMAG data processing technique. *J Geophys Res Space Phys* **117**: A09213. https://doi.org/10.1029/2012JA017683.

Gonzalez, WD, Joselyn JA, Kamide Y, Kroehl HW, Rostoker G, et al. 1994. What is a geomagnetic storm? *J Geophys Res Space Phys* **99**: 5771–5792. https://doi.org/10.1029/93JA02867.

Gonzalez, WD, Tsurutani BT. 1987. Criteria of interplanetary parameters causing intense magnetic storms (Dst < -100 nT). *Planet Space Sci* **35**: 1101–1109. https://doi.org/10.1016/0032-0633(87)90015-8.

Gonzalez-Esparza, JA, Sanchez-Garcia E, Sergeeva M, Corona-Romero P, Gonzalez-Mendez LX, et al. 2024. The Mother's Day geomagnetic storm on 10 May 2024: Aurora observations and low latitude space weather effects in Mexico. *Space Weather* **22**: e2024SW004111. https://doi.org/10.1029/2024SW004111.

Gopalswamy, N, Yashiro S, Michalek G, Xie H, Lepping RP, Howard RA. 2005. Solar source of the largest geomagnetic storm of cycle 23. *Geophys Res Lett* **32**: L12S09. https://doi.org/10.1029/2004GL021639.

Grandin, M, Bruus E, Ledvina VE, Partamies N, Barthelemy M, et al. 2024. The Gannon Storm: Citizen science observations during the geomagnetic superstorm of 10 May 2024. *Geosci Commun* **7**: 297–316. https://doi.org/10.5194/gc-7-297-2024.

Guo, J, Feng X, Emery BA, Zhang J, Xiang C, et al. 2011. Energy transfer during intense geomagnetic storms driven by interplanetary coronal mass ejections and their sheath regions: Energy transfer. *J Geophys Res Space Phys* **116**: A05106. https://doi.org/10.1029/2011JA016490.

Guo, X, Zhao B, Yu T, Hao H, Sun W, et al. 2024. East–West difference in the ionospheric response during the recovery phase of May 2024 super geomagnetic storm over the East Asian. *J Geophys Res Space Phys* **129**: e2024JA033170. https://doi.org/10.1029/2024JA033170.

Hajra, R, Echer E, Tsurutani BT, Gonzalez WD. 2014. Solar wind-magnetosphere energy coupling efficiency and partitioning: HILDCAAs and preceding CIR storms during solar cycle 23. *J Geophys Res Space Phys* **119**: 2675–2690. https://doi.org/10.1002/2013JA019646.

Hajra, R, Tsurutani BT, Lakhina GS, Lu Q, Du A. 2024a. Interplanetary causes and impacts of the 2024 May superstorm on the geosphere: An overview. *Astrophys J* **974**: 264. https://doi.org/10.3847/1538-4357/ad7462.

Hajra, R, Tsurutani BT. 2018. Interplanetary shocks inducing magnetospheric supersubstorms (SML < -2500 nT): Unusual auroral morphologies and energy flow. *Astrophys J* **858**: 123. https://doi.org/10.3847/1538-4357/aabaed.

Hajra, R, Tsurutani BT, Echer E, Gonzalez WD, Gjerloev JW. 2016. Supersubstorms (SML < -2500): Magnetic storm and solar cycle dependences. *J Geophys Res Space Phys* **121**: 7805–7816. https://doi.org/10.1002/2015JA021835.

Hajra, R, Echer E, Franco AMDS, Bolzan MJA. 2023. Earth's magnetotail variability during supersubstorms (SSSs): A study on solar wind–magnetosphere–ionosphere coupling. *Adv Space Res* **72**: 1208–1223. https://doi.org/10.1016/j.asr.2023.04.013.

Hajra, R, Tsurutani BT, Lu Q, Horne RB, Lakhina GS, et al. 2024b. The April 2023 SYM-H = -233 nT geomagnetic storm: A classical event. *J Geophys Res Space Phys* **129**: e2024JA032986. https://doi.org/10.1029/2024JA032986.

Hayakawa, H, Ebihara Y, Mishev A, Koldobskiy S, Kusano K, et al. 2025. The solar and geomagnetic storms in 2024 May: A flash data report. *Astrophys J* **979**: 49. https://doi.org/10.3847/1538-4357/ad9335.

Hsu, TS, McPherron RL. 2003. Occurrence frequencies of IMF triggered and nontriggered substorms. *J Geophys Res* **108**: 1307. https://doi.org/10.1029/2002JA009442.

Hugoniot, H. 1887. Mémoire sur la propagation des mouvements dans les corps et spécialement dans les gaz parfaits (première partie). *J École Polytech* **57**: 3–97.

Hugoniot, H. 1889. Mémoire sur la propagation des mouvements dans les corps et spécialement dans les gaz parfaits (deuxième partie). *J École Polytech* **58**: 1–125.

Iyemori, T. 1990. Storm-time magnetospheric currents inferred from mid-latitude geomagnetic field variations. *J Geomag Geoelectr* **42**: 1249–1265. https://doi.org/10.5636/jgg.42.1249.

Kennel, CF, Edmiston JP, Hada T. 1985. A quarter century of collisionless shock research. In: *Geophysical Monograph Series*, RG, Stone, Tsurutani BT (Eds.). American Geophysical Union, Washington, D.C., pp. 1–36. https://doi.org/10.1029/GM034p0001.

Knipp, DJ, Tobiska WK, Emery BA. 2004. Direct and indirect thermospheric heating sources for solar cycles 21–23. *Solar Phys* **224**: 495–505. https://doi.org/10.1007/s11207-005-6393-4.

Laitinen, J, Holappa L, Vanhamäki H. 2024. The polarity of IMF By strongly modulates particle precipitation during high-speed streams. *Geophys Res Lett* **51**: e2024GL110877. https://doi.org/10.1029/2024GL110877.

Lakhina, GS, Tsurutani BT, Kojima H, Matsumoto H. 2000. "Broadband" plasma waves in the boundary layers. *J Geophys Res Space Phys* **105**: 27791–27831. https://doi.org/10.1029/2000JA900054.

Lakhina, GS, Tsurutani BT. 2016. Geomagnetic storms: Historical perspective to modern view. *Geosci Lett* **3**: 5. https://doi.org/10.1186/s40562-016-0037-4.

Lee, W, Liu G, Wu DL, Rowland DE. 2025. Ionospheric response to the 10 May 2024 geomagnetic storm as observed in GNSS radio occultation electron density. *J Geophys Res Space Phys,* **130**: e2024JA033489. https://doi.org/10.1029/2024JA033489.

Liou, K, Sotirelis T, Mitchell E. 2020.Control of the East–West component of the interplanetary magnetic field on the occurrence of magnetic substorms. *Geophys Res Lett* **47**: e2020GL087406. https://doi.org/10.1029/2020GL087406.

Lockwood, M, Owens MJ, Brown W, Vázquez M. 2025. The 2024 May event in the context of auroral activity over the past 375 yr. *Mon Not Royal Astron Soc* **540**: 3596–3624. https://doi.org/10.1093/mnras/staf827.

Lu, Q, Fu H, Wang R, Lu S. 2022. Collisionless magnetic reconnection in the magnetosphere. *Chin Phys B* **31**: 089401. https://doi.org/10.1088/1674-1056/ac76ab.

Lu, S, Guo J, Lu Q, Shu Y, Ren J, Wang R, Hajra R. 2025. Three-dimensional global hybrid simulations of plasma transport and energy conversion during solar wind-magnetosphere interactions. *Geophys Res Lett* **52**: e2025GL117084. https://doi.org/10.1029/2025GL117084.

Marubashi, K, Lepping RP. 2007. Long-duration magnetic clouds: a comparison of analyses using torus- and cylinder-shaped flux rope models. *Ann Geophys* **25**: 2453–2477. https://doi.org/10.5194/angeo-25-2453-2007.

Nanjo, S, Shiokawa K. 2024. Spatial structures of blue low-latitude aurora observed from Japan during the extreme geomagnetic storm of May 2024. *Earth Planets Space* **76**: 156. https://doi.org/10.1186/s40623-024-02090-9.

Newell, PT, Gjerloev JW. 2011. Substorm and magnetosphere characteristic scales inferred from the SuperMAG auroral electrojet indices. *J Geophys Res* **116**: A12232. https://doi.org/10.1029/2011JA016936.

Ohma, A, Reistad JP, Hatch SM. 2021. Modulation of magnetospheric substorm frequency: Dipole tilt and IMF By effects. *J Geophys Res Space Phys* **126**: e2020JA028856. https://doi.org/10.1029/2020JA028856.

Ohtani, S. 2021. Revisiting the partial ring current model: Longitudinal asymmetry of ground magnetic depression during geomagnetic storms. *J Geophys Res Space Phys* **126**: e2021JA029643. https://doi.org/10.1029/2021JA029643.

Paul, KS, Moses M, Haralambous H, Oikonomou C. 2025. Effects of the Mother's Day superstorm (10–11 May 2024) over the global ionosphere. *Remote Sens* **17**: 859. https://doi.org/10.3390/rs17050859.

Perreault, P, Akasofu SI. 1978. A study of geomagnetic storms. *Geophys J Int* **54**: 547–573. https://doi.org/10.1111/j.1365-246X.1978.tb05494.x.

Piersanti, M, Oliveira DM, D'Angelo G, Diego P, Napoletano G, et al. 2025. On the geoelectric field response to the SSC of the May 2024 super storm over Europe. *Space Weather* **23**: e2024SW004191.

Rankine, WJM. 1870. XV. On the thermodynamic theory of waves of finite longitudinal disturbance. *Phil Trans Royal Soc* **160**: 277–288. https://doi.org/10.1098/rstl.1870.0015.

Sckopke, N. 1966. A general relation between the energy of trapped particles and the disturbance field near the Earth. *J Geophys Res* **71**: 3125–3130. https://doi.org/10.1029/JZ071i013p03125.

Spogli, L, Alberti T, Bagiacchi P, Cafarella L, Cesaroni C, et al. 2024. The effects of the May 2024 Mother's Day superstorm over the Mediterranean sector: From data to public communication. *Ann Geophys* **67**: PA218. https://doi.org/10.4401/ag-9117.

Sun, W, Li G, Zhang S, Zhao B, Li Y, et al. 2024. Complex ionospheric fluctuations over East and Southeast Asia during the May 2024 super geomagnetic storm. *J Geophys Res Space Phys* **129**: e2024JA033096. https://doi.org/10.1029/2024JA033096.

Themens, DR, Elvidge S, McCaffrey A, Jayachandran PT, Coster A, et al. 2024. The high latitude ionospheric response to the major May 2024 geomagnetic storm: A synoptic view. *Geophys Res Lett* **51**: e2024GL111677. https://doi.org/10.1029/2024GL111677.

Tsurutani, BT, Mannucci AJ, Iijima B, Abdu MA, Sobral JHA, et al. 2004. Global dayside ionospheric uplift and enhancement associated with interplanetary electric fields. *J Geophys Res Space Phys* **109**: 2003JA010342. https://doi.org/10.1029/2003JA010342.

Tsurutani, BT, Hajra R, Echer E, Gjerloev JW. 2015. Extremely intense (SML $\leq$–2500 nT) substorms: isolated events that are externally triggered? *Ann Geophys* **33**: 519–524. https://doi.org/10.5194/angeo-33-519-2015.

Tsurutani, BT, Hajra R, Tanimori T, Takada A, Remya B, et al. 2016. Heliospheric plasma sheet (HPS) impingement onto the magnetosphere as a cause of relativistic electron dropouts (REDs) via coherent EMIC wave scattering with possible consequences for climate change mechanisms. *J Geophys Res Space Phys* **121**: 10130–10156. https://doi.org/10.1002/2016JA022499.

Tsurutani, BT. 2024. A long and winding path through space weather research. *Persp Earth Space Sci* **5**: e2024CN000259. https://doi.org/10.1029/2024CN000259.

Tsurutani, BT, Gonzalez WD. 2007. A new perspective on the relationship between substorms and magnetic storms. In: *Advances in geosciences*, **Vol. 8: Solar Terrestrial (ST)**, World Scientific Publishing Co. Pte. Ltd., Singapore, pp. 25–45. https://doi.org/10.1142/9789812708939_0002.

Tsurutani, BT, Hajra R. 2023. Energetics of shock-triggered supersubstorms (SML $<$ -2500 nT). *Astrophys J* **946**: 17. https://doi.org/10.3847/1538-4357/acb143.

Tsurutani, BT, Lin RP. 1985. Acceleration of >47 keV Ions and >2 keV electrons by interplanetary shocks at 1 AU. *J Geophys Res* **90**: 1–11. https://doi.org/10.1029/JA090iA01p00001.

Tsurutani, BT, Gonzalez WD, Tang F, Akasofu SI, Smith EJ. 1988. Origin of interplanetary southward magnetic fields responsible for major magnetic storms near solar maximum (1978–1979). *J Geophys Res* **93**: 8519–8531. https://doi.org/10.1029/JA093iA08p08519.

Tsurutani, BT, Sen A, Hajra R, Lakhina GS, Horne RB, et al. 2024. Review of the August 1972 and March 1989 (Allen) space weather events: Can we learn anything new from them? *J Geophys Res Space Phys* **129**: e2024JA032622. https://doi.org/10.1029/2024JA032622.

Tsurutani, BT, Lakhina GS, Verkhoglyadova OP, Gonzalez WD, Echer E, et al. 2011. A review of interplanetary discontinuities and their geomagnetic effects. *J Atmos Solar-Terr Phys* **73**: 5–19. https://doi.org/10.1016/j.jastp.2010.04.001.

Turner, NE, Mitchell EJ, Knipp DJ, Emery BA. 2006. Energetics of magnetic storms driven by corotating interaction regions: A study of geoeffectiveness. In : *Geophysical Monograph Series*, **Vol. 167**, BT, Tsurutani, McPherron R, Gonzalez W, Lu G, Sobral JHA, Gopalswamy N (Eds.). American Geophysical Union, Washington, D.C., pp. 113–124. https://doi.org/10.1029/167GM11.

Wang, H, Cheng Q, Lühr H, Zhong Y, Zhang K, et al. 2024. Local time and hemispheric asymmetries of field-aligned currents and polar electrojet during May 2024 superstorm periods. *J Geophys Res Space Phys* **129**: e2024JA033020. https://doi.org/10.1029/2024JA033020.

West, HI, Buck RM, Walton JR. 1972. Shadowing of electron azimuthal-drift motions near the noon magnetopause. *Nature Phys Sci* **240**: 6–7. https://doi.org/10.1038/physci240006a0.

West, HI, Buck RM, Davidson GT. 1981.The dynamics of energetic electrons in the Earth's outer radiation belt during 1968 as observed by the Lawrence livermore National Laboratory's spectrometer on Ogo 5. *J Geophys Res Space Phys* **86**: 2111–2142. https://doi.org/10.1029/JA086iA04p02111.

Yokoyama, N, Kamide Y. 1997. Statistical nature of geomagnetic storms. *J Geophys Res Space Phys* **102**: 14215–14222. https://doi.org/10.1029/97JA00903.

Zhou, X, Tsurutani BT. 1999. Rapid intensification and propagation of the dayside aurora: Large scale interplanetary pressure pulses (fast shocks). *Geophys Res Lett* **26**: 1097–1100. https://doi.org/10.1029/1999GL900173.

Zhou, X, Tsurutani BT. 2001. Interplanetary shock triggering of nightside geomagnetic activity: Substorms, pseudobreakups, and quiescent events. *J Geophys Res Space Phys* **106**: 18957–18967. https://doi.org/10.1029/2000JA003028.

Zou, Y, Shin O, Gjerloev JW, Anderson BJ, Waters CL, et al. 2025. Are supersubstorms substorms? Extreme nightside auroral electrojet activities during the May 2024 geomagnetic storm. *J Geophys Res Space Phys* **130**: e2024JA033303. https://doi.org/10.1029/2024JA033303.

Cite this article as: Hajra R, Tsurutani B, Lu Q, Du A & Lakhina G. 2025. Supersubstorms during the May 2024 superstorm. *J. Space Weather Space Clim.* **15**, 51. https://doi.org/10.1051/swsc/2025047.

Appendix A: Magnetic local time dependence of the SSSs

Figure A1 shows MLT dependence of SML variations during the six SSSs under this study. While the SSS SML strength is determined from the total SML index (shown by solid lines), MLT-UT contour plots indicate significant MLT dependence of SML during the SSSs. The SSS 1 and SSS 2 peaks are associated with the strongest SML values around 06:00–10:00 MLT (Fig. A1a), the SSS 5 and SSS 6 with the strong SML values around 02:00–10:00 MLT (Fig. A1c). However, the SSS 3 and SSS 4 are associated with SML intensifications from ~20:00 to ~08:00 MLT (Fig. A1b). Thus, the SML intensifications during SSS 1, SSS 2, SSS 5, and SSS 6 are mainly contributed by the magnetic daytime ionosphere, while those during SSS 3 and SSS 4 are contributed by the magnetic nighttime ionosphere.

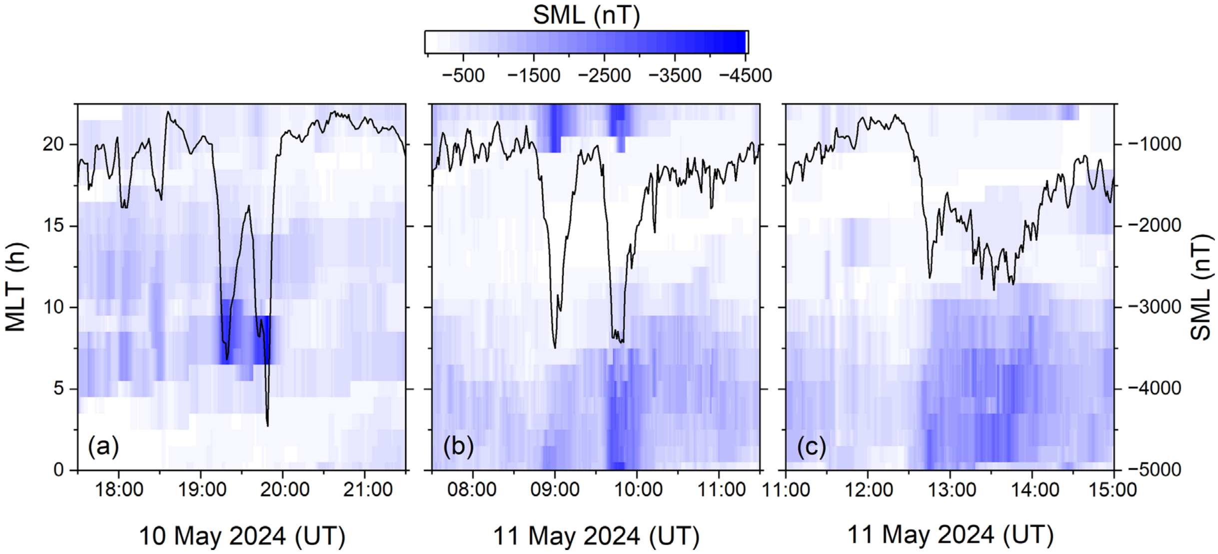

Figure A1. MLT dependence of SML during the six SSSs. MLT-UT contour plots show variations of SML associated with the SSSs during 10–11 May 2024. The SML values corresponding to different colors are shown by the color bar at the top. On each plot superposed are the UT variations of total SML indices, legend on the right.

Appendix B: Energy coupling

Figure B1 shows the energy input and dissipated rates during 10–11 May 2024. The IMF magnitude and components, and the SYM-H and SML indices are shown for reference. The JH rate (Fig. B1c) is ~1 order of magnitude larger than the RC and AP rates (Fig. B1c). Thus, we omitted RC and AP from the substorm energy budget discussion in the main text.

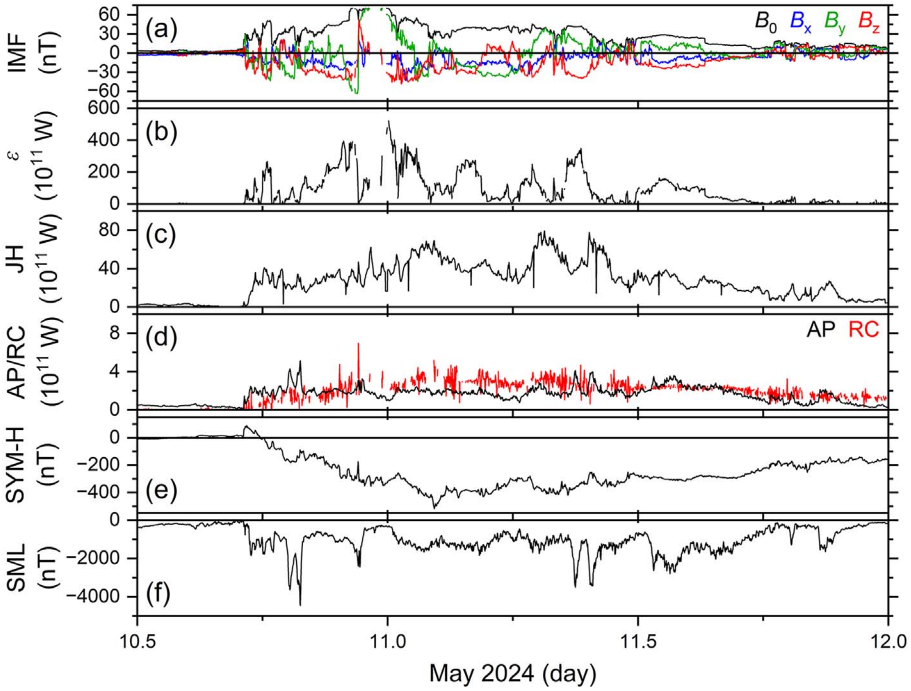

Figure B1. Magnetosphere-ionosphere energy coupling during 10–11 May 2024. From top to bottom, panels are: (a) IMF B_0, and B_x, B_y, B_z components, (b) Akasofu ε-parameter, (c) the total JH rate, (d) rates of auroral precipitation AP, and ring current dissipation RC, (e) SYM-H, and (f) SML.